

# Importance of the initial conditions for star formation – II. Fragmentation-induced starvation and accretion shielding

Philipp Girichidis,<sup>1,2,3★</sup> Christoph Federrath,<sup>1,4,5</sup> Robi Banerjee<sup>3</sup> and Ralf S. Klessen<sup>1</sup>

<sup>1</sup>*Institut für Theoretische Astrophysik, Zentrum für Astronomie der Universität Heidelberg, Albert-Ueberle-Str. 2, 69120 Heidelberg, Germany*

<sup>2</sup>*Cardiff School of Physics and Astronomy, The Parade, Cardiff CF24 3AA*

<sup>3</sup>*Hamburger Sternwarte, Gojenbergsweg 112, 21029 Hamburg, Germany*

<sup>4</sup>*Ecole Normale Supérieure de Lyon, CRAL, 69364 Lyon Cedex 07, France*

<sup>5</sup>*Monash Centre for Astrophysics (MoCA), School of Mathematical Sciences, Monash University, Vic 3800, Australia*

Accepted 2011 October 25. Received 2011 October 24; in original form 2011 June 3

## ABSTRACT

We investigate the impact of different initial conditions for the initial density profile and the initial turbulence on the formation process of protostellar clusters. We study the collapse of dense molecular cloud cores with three-dimensional adaptive mesh refinement simulations. We focus our discussion on the distribution of the gas among the protostellar objects in the turbulent dynamical cores. Despite the large variations in the initial configurations and the resulting gas and cluster morphology we find that all stellar clusters follow a very similar gas accretion behaviour. Once secondary protostars begin to form, the central region of a cluster is efficiently shielded from further accretion. Hence, objects located close to the centre are starved of material, as indicated by a strong decrease of the central accretion rate. This fragmentation-induced starvation occurs not only in rotationally supported discs and filaments, but also in more spherically symmetric clusters with complex chaotic motions.

**Key words:** hydrodynamics – instabilities – turbulence – stars: formation.

## 1 INTRODUCTION

The current paradigm of star formation suggests that most stars form in groups rather than in isolation (Lada et al. 2003). However, the fraction of stars that form in a bound clustered environment is still a matter of debate and varies between different models (Bressert et al. 2010). Whereas massive stars only seem to form in a dense environment, low-mass stars form in all observed star-forming regions. Numerical simulations suggest the formation of massive stars simultaneously with the formation of a cluster (Smith, Longmore & Bonnell 2009; Peters et al. 2010a,b,c). The spatial distribution of stars in the forming cluster shows a dependence on the stellar mass: more massive stars are located closer to the centre of the group, low-mass stars tend to populate the outer regions. Whether this mass segregation is primordial and therefore determined by the formation scenario or due to a dynamical relaxation process is still a matter of debate and might differ significantly among different clusters (see e.g. the reviews by Mac Low & Klessen 2004; McKee & Ostriker 2007; Zinnecker & Yorke 2007). Commonly found in observations as well as in numerical simulations is a universal distribution of masses [initial mass function (IMF); Scalo 1986, 1998; Kroupa 2001; Chabrier 2003; Bastian, Covey & Meyer 2010]. Yet

it is unclear, what is the influence of various physical processes and initial conditions on the initial mass distribution in star-forming regions. Different physical processes like radiative feedback and magnetic fields are likely to have an impact on the collapse of gas clouds and the subsequent formation of a stellar cluster. Radiative feedback from protostars can have two opposite effects. On the one hand, it heats the surrounding gas and thus contributes to stabilizing the gas against collapse by increasing the Jeans mass. In case of massive protostars, the strong contribution in ultraviolet (UV) ionizes the gas, forming H II regions. Hydrodynamic simulations of forming clusters show that radiative feedback tends to reduce the degree of fragmentation, but does not suppress it entirely (Krumholz, Klein & McKee 2007; Bate 2009; Peters et al. 2010a,b,c). On the other hand, radiation pressure may indirectly enhance the formation of dense cores and the subsequent condensation into protostars. There are two different scenarios for this triggered star formation process. The first, ‘collect and collapse’ (Elmegreen & Lada 1977; Whitworth et al. 1994), appears where an expanding H II region pushes ambient gas into a shell, followed by fragmentation and collapse of the swept-up material. The other one is called ‘radiation-driven implosion’ (Bertoldi 1989; Bertoldi & McKee 1990) and depicts the UV-driven compression of a cloud core that is embedded into an H II region. Apart from radiation, magnetic fields have a noticeable impact on the evolution of a collapsing core. Magnetic pressure and tension forces counter the gravitational

★E-mail: philipp@girichidis.com

collapse and diminish fragmentation without completely inhibiting it (Ziegler 2005; Banerjee & Pudritz 2006; Price & Bate 2007; Hennebelle & Fromang 2008; Hennebelle & Teyssier 2008; Hennebelle & Ciardi 2009; Commerçon et al. 2010; Bürzle et al. 2011; Seifried et al. 2011). Likewise, different initial conditions of the gas cloud strongly influence the star formation process (Girichidis et al. 2011, hereafter Paper I).

However, a clear universal formation picture of stellar systems in dense environments is still missing. Several formation and gas accretion processes have been proposed with different distribution scenarios of the gas on to the protostellar objects and different predictions concerning the more massive stars and the resulting IMF. The apparent similarity between the stellar mass function and the mass function of bound cores (Testi & Sargent 1998) lead to the monolithic collapse model as a possible star formation scenario, in which every dense protostellar core collapses to a single star (McKee & Tan 2002, 2003). However, this scenario leads to a time-scale problem that can effectively destroy the similarity between IMF and the core mass function (Clark, Klessen & Bonnell 2007). Similar problems hold for the proposal that massive stars form by collisions of low-mass stars (Zinnecker & Yorke 2007), because the observed stellar densities are too low for this process to be important (Baumgardt & Klessen 2011). As the formation process of a cluster in a dense environment is highly turbulent and dynamic, analytic estimates only give a vague idea of how accretion in these surroundings may work. With the help of simulations, two different cases have been proposed. In one scenario, which is called competitive accretion, the formation of the most massive stars is due to a privileged position close to the centre of the stellar cluster, where the accretion rates are predicted to be highest throughout the simulation (Bonnell et al. 2001a,b). The other scenario is fragmentation-induced starvation (Peters et al. 2010c), in which initially the central accretion rates are highest as well. However, subsequent fragmentation shows an increasing impact of the nascent protostars on the accretion behaviour of the central region that gets starved of material by the surrounding companions.

In this study we investigate the accretion process in different initial density profiles and different turbulent velocity fields. Paper I focused on the cloud structure and morphology. In this paper we investigate the accretion processes in the formed clusters in detail.

## 2 NUMERICAL METHODS AND INITIAL CONDITIONS

The simulation data used in this study are the same as in Paper I, where a detailed description of the initial set-ups can be found. Here we only summarize the key parameters.

### 2.1 Global simulation parameters

We simulate the collapse of an spherically symmetric molecular cloud with a radius of  $R = 0.1$  pc and a total mass of  $100 M_{\odot}$ . The resulting average density is  $\langle \rho \rangle = 1.76 \times 10^{-18} \text{ g cm}^{-3}$  and the corresponding free-fall time gives  $t_{\text{ff}} = 5.02 \times 10^4$  yr. The gas with a mean molecular weight of  $\mu = 2.3$  is assumed to be isothermal at a temperature of 20 K, yielding a constant sound speed of  $c_s = 2.68 \times 10^4 \text{ cm s}^{-1}$ . The Jeans length,  $\lambda_J$ , and the corresponding Jeans mass,  $M_J$ , calculated as a sphere with diameter  $\lambda_J$ , are  $\lambda_J = 9300$  au and  $M_J = 1.23 M_{\odot}$ , respectively. Table 1 provides an overview of all physical parameters.

**Table 1.** Physical parameters of all set-ups.

Parameter		Value
Cloud radius	$R$	$3 \times 10^{17} \text{ cm} \approx 0.097 \text{ pc}$
Total cloud mass	$M_{\text{tot}}$	$100 M_{\odot}$
Mean mass density	$\langle \rho \rangle$	$1.76 \times 10^{-18} \text{ g cm}^{-3}$
Mean number density	$\langle n \rangle$	$4.60 \times 10^5 \text{ cm}^{-3}$
Mean molecular weight	$\mu$	2.3
Temperature	$T$	20 K
Sound speed	$c_s$	$0.27 \text{ km s}^{-1}$
rms Mach number	$\mathcal{M}$	3.28–3.64
Mean free-fall time	$t_{\text{ff}}$	$5.02 \times 10^4 \text{ yr}$
Sound crossing time	$t_{\text{sc}}$	$7.10 \times 10^5 \text{ yr}$
Turbulent crossing time	$t_{\text{tc}}$	$1.95\text{--}2.16 \times 10^5 \text{ yr}$
Jeans length	$\lambda_J$	$9.26 \times 10^3 \text{ au} \approx 0.23 R_0$
Jeans volume	$V_J$	$1.39 \times 10^{51} \text{ cm}^3$
Jeans mass	$M_J$	$1.23 M_{\odot}$

### 2.2 Numerical code

The simulations were carried out with the astrophysical code FLASH (Fryxell et al. 2000) in version 2.5. To integrate the hydrodynamic equations, we use a piecewise-parabolic method (PPM; Colella & Woodward 1984). The code is parallelized using MPI. The computational domain is subdivided into blocks containing a fixed number of cells with an adaptive mesh refinement (AMR) technique based on the PARAMESH library (Olson et al. 1999).

### 2.3 Resolution and sink particles

The simulations were run with a maximum effective resolution of  $4096^3$  grid cells, corresponding to a smallest cell size of  $\Delta x \approx 13$  au. In order to avoid artificial fragmentation, the Jeans length has to be resolved with at least four grid cells (Truelove et al. 1997). At the highest level of refinement, we set the minimum resolution of the Jeans length to  $6\Delta x$ , which can be transformed to a maximum density of

$$\rho_{\text{max}} = \frac{\pi c_s^2}{4G(3\Delta x)^2} = 2.46 \times 10^{-14} \text{ g cm}^{-3}. \quad (1)$$

On all lower levels of refinement, the Jeans length is resolved with at least eight grid cells. If a cell exceeds this density, a spherical control volume with a radius of  $3\Delta x$  is investigated for gravitational collapse indicators. If the collapse criteria (Federrath et al. 2010a) are fulfilled, an accreting Lagrangian sink particle is formed. While the total mass of the collapsing control volume is of the order of a Jeans mass at that density, the initial mass of the sink particle is only the mass corresponding to the overdensity above the maximum gas density  $\rho_{\text{max}}$ . Therefore, the initial mass of the sink particle at the time of formation is typically significantly below the Jeans mass, and can be as low as  $10^{-6} M_{\odot}$ . Table 2 lists the simulation and resolution parameters.

### 2.4 Initial conditions

The following four density profiles were used:

- (i) top-hat profile,  $\rho = \text{const}$  (TH);
- (ii) rescaled Bonnor–Ebert sphere (BE);
- (iii) power-law profile,  $\rho \propto r^{-1.5}$  (PL15);
- (iv) power-law profile,  $\rho \propto r^{-2.0}$  (PL20).

A detailed description of the profiles can be found in Paper I.

**Table 2.** Numerical simulation parameters.

Parameter		Value
Simulation box size	$L_{\text{box}}$	0.26 pc
Smallest cell size	$\Delta x$	13.06 au
Jeans length resolution		$\geq 8(6^a)$ cells
Max. gas density	$\rho_{\text{max}}$	$2.46 \times 10^{-14} \text{ g cm}^{-3}$
Max. number density	$n_{\text{max}}$	$6.45 \times 10^9 \text{ cm}^{-3}$
Sink particle accretion radius	$r_{\text{accr}}$	39.17 au

<sup>a</sup> At highest level of refinement.

The turbulence is modelled with an initial random velocity field, originally created in Fourier space and transformed back into real space. The power spectrum of the modes is given by a power-law function in wavenumber space ( $\mathbf{k}$  space) with  $E_k \propto k^{-2}$ , corresponding to Burgers turbulence, consistent with the observed spectrum of interstellar turbulence (e.g. Larson 1981; Heyer & Brunt 2004). The velocity field is dominated by large-scale modes due to the steep power-law exponent,  $-2$ , with the largest mode corresponding to the size of the simulation box. Concerning the nature of the  $\mathbf{k}$  modes, compressive (curl-free) modes are distinguished from solenoidal (divergence-free) ones. The simulation uses three types of initial fields: purely compressive fields (c), purely solenoidal (s) and a natural (random) mixture (m) of both. The choice of these different turbulent fields was motivated by the strong impact of the nature of the modes on the cloud evolution, found by Federrath, Klessen & Schmidt (2008) and Federrath et al. (2010b). Notice also that the scale of the turbulence influences the result significantly (Klessen, Heitsch & Mac Low 2000), with most realistic results corresponding to large-scale driving adopted here (Klessen 2001), where we focus on decaying turbulence with compressive, solenoidal and mixed modes are considered here.

All set-ups have supersonic velocities with an rms Mach number  $\mathcal{M} = v_{\text{rms}}/c_s$  ranging from  $\mathcal{M} = 3.28$  to  $3.54$  with an average of  $\langle \mathcal{M} \rangle = 3.44$ . The sound crossing time through the entire cloud is

$t_{\text{sc}}(R) = 7.10 \times 10^5 \text{ yr}$ , and the time for gas with an average velocity of  $\langle \mathcal{M} \rangle c_s$  to cross the cloud is  $t_{\text{ic}}(R) = 2.06 \times 10^5 \text{ yr}$ , respectively.

We do not explicitly impose any rotation on the cloud. Because of the initial turbulence and randomly located velocity patterns in regions with different density, the total net rotational energy does not strictly vanish. However, the ratio  $E_{\text{rot}}/|E_{\text{pot}}|$  is less than a few times  $10^{-3}$ , so only very little energy is deposited in global net rotation.

We combine four density profiles with six different turbulent velocity fields (three different compositions of modes with two different random seeds each). Table 3 shows a list of all models.

### 3 RESULTS

#### 3.1 Overview

We follow the cloud collapse until 20 per cent of the mass is accreted by sink particles. The simulation time, the number of formed protostars and the mass of the most massive protostar are listed in Table 3. A column density plot at the end of each simulation is shown in Paper I (figs 4 and 5).

The TH profile needs the longest time to form collapsing overdensities and confine  $20 M_{\odot}$  in sink particles. During this time of about 45 kyr, the turbulent motions can compress the gas in locally disconnected areas, leading to distinct subclusters of sink particles. The stronger mass concentration in the centre of the BE set-ups and the resulting shorter collapse and sink particle formation time suppresses the formation of disconnected subclusters in favour of one main central cluster. The corresponding PL15 profiles show very similar cloud structure to the BE runs, but significantly different stellar properties. Because of the much stronger gas concentration in the centre of the cloud, all PL15 set-ups form one sink particle very early in the simulation. This central sink particle accretes the surrounding gas at a high rate and can grow to a massive protostar before the turbulent motions eventually trigger the formation of collapsing filaments, which produce subsequent sink particles. Because

**Table 3.** List of the runs and their main simulation properties.

$\rho$	Turb. mode	Seed	Name	$E_{\text{kin}}/ E_{\text{pot}} $	$t_{\text{sim}}$ (kyr)	$t_{\text{sim}}/t_{\text{ff}}$	$N_{\text{sink}}$	$M_{\text{mm}}$ ( $M_{\odot}$ )
TH	Mix	1	TH-m-1	0.075	48.01	0.96	311	0.86
TH	Mix	2	TH-m-2	0.090	45.46	0.91	429	0.74
BE	Com	1	BE-c-1	0.058	27.52	0.55	305	0.94
BE	Com	2	BE-c-2	0.073	27.49	0.55	331	0.97
BE	Mix	1	BE-m-1	0.053	30.05	0.60	195	1.42
BE	Mix	2	BE-m-2	0.074	31.94	0.64	302	0.54
BE	Sol	1	BE-s-1	0.055	30.93	0.62	234	1.14
BE	Sol	2	BE-s-2	0.074	35.86	0.72	325	0.51
PL15	Com	1	PL15-c-1	0.056	25.67	0.51	194	8.89
PL15	Com	2	PL15-c-2	0.068	25.82	0.52	161	12.3
PL15	Mix	1	PL15-m-1	0.050	23.77	0.48	1	20.0
PL15	Mix	2	PL15-m-2	0.071	31.10	0.62	308	6.88
PL15	Sol	1	PL15-s-1	0.053	24.85	0.50	1	20.0
PL15	Sol	2	PL15-s-2	0.069	35.96	0.72	422	4.50
PL20	Com	1	PL20-c-1	0.042	10.67	0.21	1	20.0

*Note.* The table shows the set-ups with their turbulent modes, the random seed for the velocity field and their acronym used in further discussions. The ratio of kinetic to potential energy results from the applied scaling of the turbulent velocity and varies due to the random position of high- and low-velocity regions. The simulation time is given as total time in kyr and in units of the global free-fall time,  $t_{\text{sim}}/t_{\text{ff}}$ . The last two columns show the total number of sink particles  $N_{\text{sink}}$  and most massive particle  $M_{\text{mm}}$ , respectively.

of the stronger mass concentration, the clusters in the PL15 runs are more compact. In both cases (PL15 and BE), star formation can proceed from inside out. The central region, which is much denser in the PL15 case, forms collapsing filaments earlier. As time proceeds, the turbulence can continuously compress material in outer regions, and thus form sink particles at larger distances from the centre. The PL20 profile only forms one single sink particle due to the very strong mass concentration. It forms very early in the simulation and accretes gas at a constant rate of about  $2 \times 10^{-3} M_{\odot} \text{ yr}^{-1}$ , extremely close to the analytical value of a highly unstable singular isothermal sphere (Paper I). This results in a total simulation time of only 11 kyr, which is not enough for turbulent motions to form other filaments and further sink particles.

For the analysis of the accretion behaviour in a dense cluster environment, we only consider the set-ups with multiple sink particles. In order to understand the accretion process, especially during the early phases of a cluster, one has to distinguish between different star formation scenarios and the resulting cloud morphology around the accreting protostars. Here we discuss two extreme cases, an early disc-like structure around a central protostellar object and an initially filamentary structure that is not dominated by angular momentum. The first case is more pronounced in centrally concentrated density profiles where a net angular momentum with respect to the centre of mass is concentrated in a smaller and denser region. In contrast, initially flatter density structures allow the formation of very massive filaments and subsequently collapsing regions within these filaments out to larger distances from the centre of mass. The angular momentum with respect to the centre of mass may be of the same order as in the former case. However, due to the overall shallower density profile in the centre, the mass infall is slower and the time-scale for the formation of a disc in the central region is larger than the time-scale for turbulence to form filaments.

### 3.2 Limiting accretion effects

Before we discuss the two extreme cluster formation modes and their resulting accretion behaviour, we want to mention two effects that may limit the accretion in a cluster, namely the angular momentum barrier and accretion shielding by companion stars. In order to be accreted on to the surface of a protostar the gas needs to have a specific angular momentum that is lower than the Keplerian angular momentum with respect to the centre of the potential, given by  $j_{\text{Kepler}} = \sqrt{2GM_{\text{enc}}r}$ , where  $G$  is Newton's constant and  $M_{\text{enc}}$  is the enclosed mass within radius  $r$ . In a cluster and especially in disc-like environments, angular momentum can quickly be redistributed due to local instabilities, turbulent motions and strong accretion streams. We analyse the angular momentum of the cloud with respect to the centre of the cluster and calculate the magnitude of the average angular momentum over thin spherical shells.

For the effects of accretion shielding by surrounding companion stars, we estimate how much of the infalling gas can be accreted by secondary cluster members before reaching the centre of the cluster and becoming accreted by the primary cluster stars. Assuming a virialized cluster, one can derive the shielded fraction  $S$  using Bondi–Hoyle accretion (Bondi & Hoyle 1944; Bondi 1952). The Bondi–Hoyle radius can be written as

$$R_{\text{BH}} = \frac{2GM}{c_s^2 + v^2}, \quad (2)$$

where  $M$  is the mass of the accreting star,  $c_s$  is the speed of sound and  $v$  is the relative velocity between the star and the immediate surrounding gas. In our analysis we investigate the gas within a

radius  $r_{\text{sur}} = 100 \text{ au}$  around each protostar. An application of the Bondi–Hoyle analysis to the accretion in clusters and the cluster dynamics can also be found in Bonnell et al. (2001a). The total shielded fraction of the gas falling on to a cluster with  $N$  stars, an average stellar mass  $M$  and a cluster radius  $R_{\text{Cl}}$  can be estimated by the fraction of the shielded surface area:

$$S = \frac{4\pi N R_{\text{BH}}^2}{4\pi R_{\text{Cl}}^2} = \frac{N}{R_{\text{Cl}}^2} \left( \frac{2GM}{c_s^2 + v^2} \right)^2. \quad (3)$$

In the case of high relative velocities between the stars and the gas, the  $c_s^2$  term can be neglected. Replacing  $v$  with the global virial velocity  $v_{\text{glob}}$  of the cluster,

$$v_{\text{glob}} = \left( \frac{GM_{\text{Cl}}}{R_{\text{Cl}}} \right)^{1/2} = \left( \frac{GNM}{R_{\text{Cl}}} \right)^{1/2}, \quad (4)$$

with  $M_{\text{Cl}} = NM$  being the cluster mass (assuming equal-mass stars for simplicity), yields

$$S \propto \frac{1}{N}. \quad (5)$$

In that case, the shielding is less efficient the more stellar objects there are in the cluster. Although this might sound counterintuitive, the assumption of virial velocities for the stars explains the strongly reduced Bondi–Hoyle radius with increasing number  $N$ . In the other extreme case of no relative velocity of the star to the surrounding gas, the shielding becomes

$$S = \frac{N R_{\text{BH}}^2}{R_{\text{Cl}}^2} \propto \frac{NM^2}{c_s^2 R_{\text{Cl}}}, \quad (6)$$

linearly increasing with  $N$ . In our simulations we observe stars forming inside filaments with initially no or very small relative velocity between them and the surrounding gas. The closer to the centre the stars form or migrate during the collapse of the cloud, the more they decouple dynamically from the gas forming a strongly interacting  $N$ -body system with a gaseous background. We therefore expect the first case ( $S \propto 1/N$ ) to be more important in the central region of the cluster, whereas the latter effect ( $S \propto N$ ) is expected to be dominant in the outskirts of the cluster and in the filaments. An analysis of the simulation is shown below, separately for the two extreme formation modes.

### 3.3 Disc-like accretion mode

In the first case we discuss the accretion scenario in a disc-like structure, concentrating on simulation PL15-m-2 as an example. A global accretion history for all protostars is shown in Fig. 1, where we plot the total number of sink particles as well as the accretion rate and the total mass confined in sink particles. The middle panel shows the total accretion rate on to all sink particles  $\dot{M}_{\text{tot}}$ , the average accretion rate per protostar  $\langle \dot{M} \rangle = \dot{M}_{\text{tot}}(t)/N_{\text{sink}}(t)$ , as well as the accretion rate of the most massive protostar  $\dot{M}_{\text{mm}}$ , which happens to be the protostar located close to the centre of mass of the gas cloud and the cluster.

During the first 7 kyr, the turbulent motions do not have enough time to significantly disturb the cloud. The anisotropies formed so far can be neglected and the assumption of an spherically symmetric collapse holds. The first sink particle forms in the centre of the cloud and accretes material in nearly free-fall. The initial density profile results in a linearly increasing accretion rate (see also Klessen, Heitsch & Mac Low 2000; Schmeja & Klessen 2004). At around  $t \sim 7 \text{ kyr}$ , the turbulent motions form a central filament whose colliding arms concentrate angular momentum in the gas around the



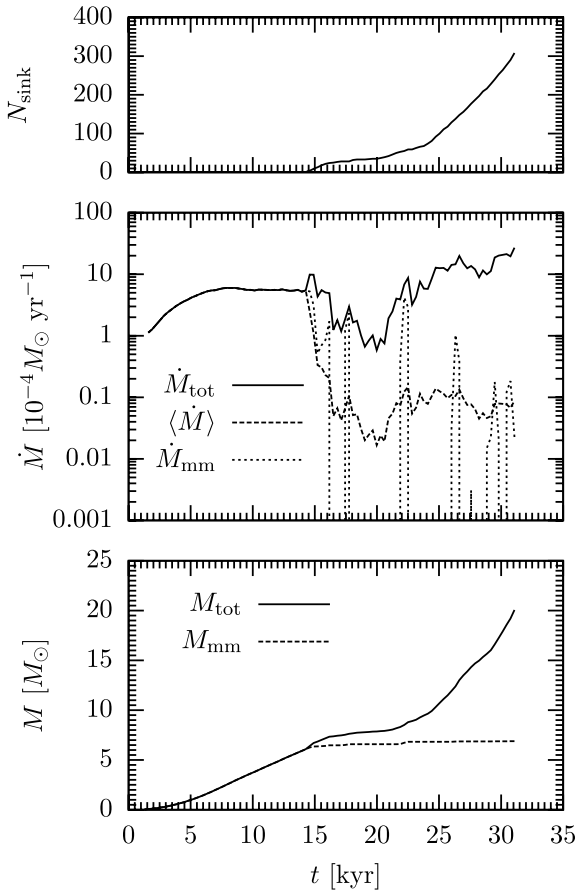


**Figure 1.** Mass evolution of the most massive, central sink particle in set-up PL15-m-2. The upper panel shows the number of sink particles in the set-up, the middle panel plots the accretion rate on to the most massive sink particle ( $\dot{M}_{\text{mm}}$ ) and on to all sink particles ( $\dot{M}_{\text{tot}}$ ). The bottom panel shows the mass.

central protostar and form a disc-like object. Thus, the spherically symmetric free-fall approximation does not hold any longer. For the time in range  $7 \lesssim t \lesssim 14$  kyr the disc is stable and grows in mass and size by accretion from the filamentary arms. During that time, the angular momentum barrier prevents the accretion rate to increase further, resulting in a constant value of  $\dot{M} \approx 5 \times 10^{-4} M_{\odot} \text{ yr}^{-1}$ . At  $t \gtrsim 14$  kyr, the disc becomes unstable, forms spiral arms and fragments into multiple objects. The column density plots in Fig. 2 show a time sequence of this short period. After the formation of other protostars, the accretion rate on to the central sink particle drops dramatically, while the total accretion rate on to all sink particles increases. The gravitational interactions between the protostars in combination with further infalling gas from the filament disturb the initially disc-like structure and quickly destroy the disc. As a result, a more or less spherically symmetric cluster builds up. The average accretion rate  $\langle \dot{M} \rangle$  decreases by more than an order of magnitude after the formation of secondary stars. The fact that  $\dot{M}_{\text{mm}}$  is on average several orders of magnitude lower than  $\langle \dot{M} \rangle$  indicates that the available gas is not equally shared among the protostars but efficiently shielded from reaching the central region. This indicates that the process of fragmentation-induced starvation, first described by Peters et al. (2010c) for disc-like structures, also works for more complex geometries. Small amounts of gas that can penetrate through the entire cluster and reach the centre can be seen as episodic accretion spikes.

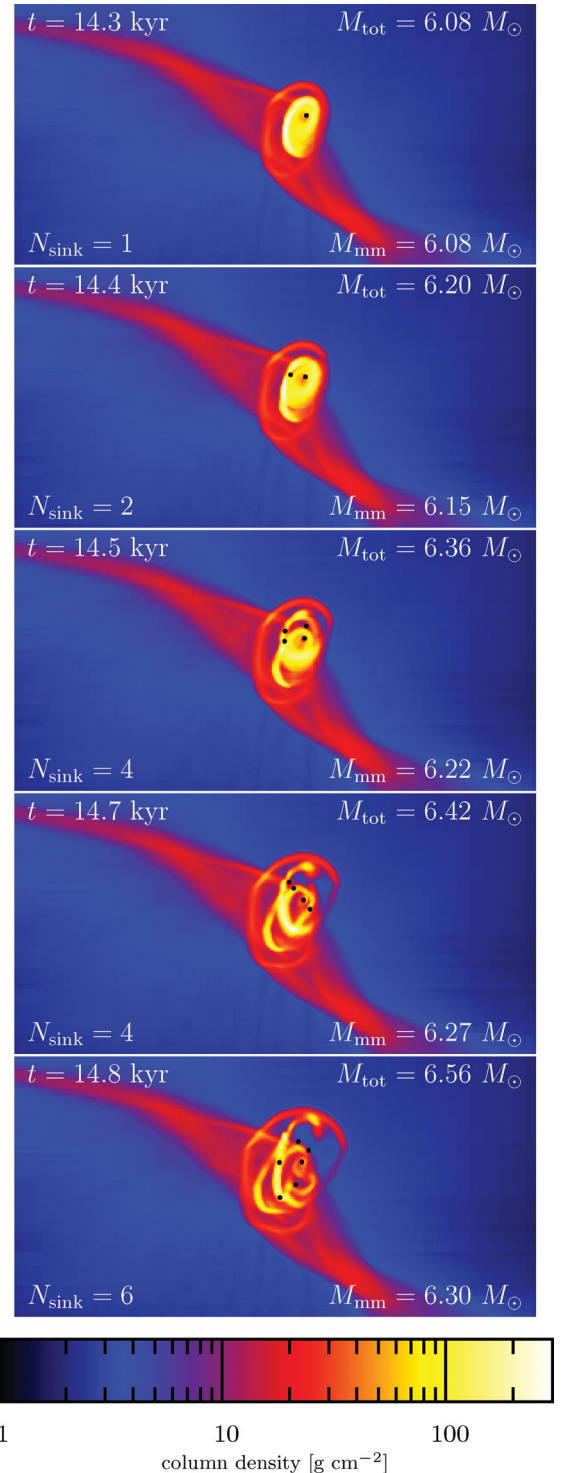


**Figure 2.** Column density plots of the central region with the disc around the most massive sink particle (subscript mm) in run PL15-m-2. The formation of secondary sink particles indicates the fragmentation into several objects, which quickly leads to the dissolution of the disc. Spiral arms develop and redirect the gas away from the central protostar, which gets starved of material. The images span roughly  $4000 \times 2000$  au.

We emphasize the influence of different geometrical shapes of the cluster. Whereas in Peters et al. (2010c) the angular momentum vector was well defined and the starvation effect was complete, the turbulent motions in our simulation allow for some accretion

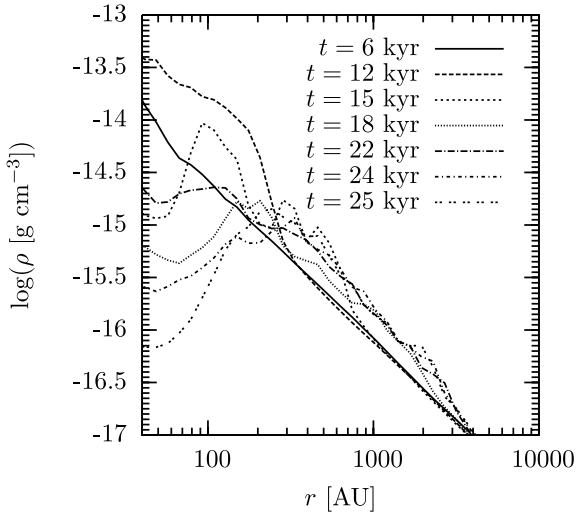


**Figure 3.** Radial density profile around the central protostar in run PL15-m-2. The gas density first increases in the immediate proximity of the protostar due to the global infall. At later times, the surrounding companions branch off most of the gas, leading to a continuous decrease of the central gas density.

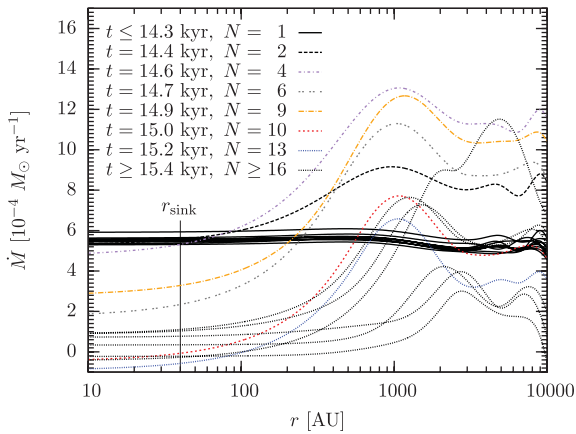


**Figure 4.** Accretion rate on to spherical shells around the central protostar in the cluster of set-up PL15-m-2. The sink particle's accretion radius is indicated by  $r_{\text{sink}}$ . The plot shows several curves for  $t \leq 14.3$  kyr, where there is only one sink particle ( $N = 1$ ). Before the formation of secondary protostars, the accretion rate in the centre is roughly constant. Immediately after surrounding companions have formed, the accretion front moves to larger radii and starves the central object. At later simulation times ( $t \geq 15.4$  kyr) the accretion rate varies, but stays very small for all curves.

channels. The starvation effect can be understood by plotting the gas density around the central protostar (Fig. 3) and the accretion rate on to spherical shells around the central protostar (Fig. 4), including the net accretion on to gas shells as well as the accretion on to other sink particles. The gas density within a radius of  $r \sim 300$  au around the central protostar first increases due to the global infall, forming a dense disc. Once other companions have formed, it decreases continuously, which starves the central object. The accretion rate as a function of radius supports this starvation picture. Before subsequent sink particles form, the accretion rate is roughly constant ( $\dot{M} \approx 5 \times 10^{-4} M_{\odot} \text{ yr}^{-1}$ ). Immediately after the disc fragments, the accretion front moves outwards to larger radii, resulting in significantly smaller values around the central protostar. As the protostars in the cluster as well as the gas undergo strong

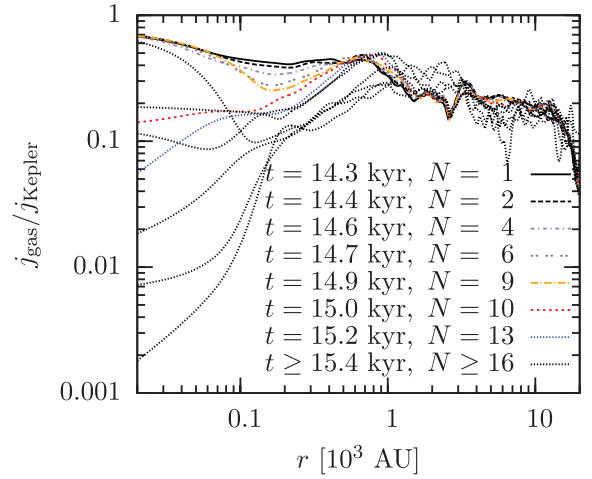


**Figure 5.** Ratio of specific angular momentum of the gas to the Keplerian value with respect to the centre of the cluster. For all times and all radii the ratio is smaller than unity, indicating that the gas is not prevented from moving inwards by angular momentum. After the formation of subsequent protostars the efficient angular momentum transport even lowers the ratio close to the centre.

dynamical interactions, the net accretion rate exhibits local fluctuations. The curves for  $t \geq 15.4$  kyr are therefore averaged over several thousand years. Phases that include an accretion spike (see second panel in Fig. 2) lead to positive values at  $r_{\text{sink}}$ , at other times the net accretion is negative, because some gas that is not bound to a protostar can enter and exit a spherical shell without being accreted on to any protostar. During the entire simulation time, but in particular after the formation of subsequent protostars, the specific angular momentum in the disc-like object (see Fig. 2) as well as in the later formed spherically symmetric cluster is lower than the Keplerian value for all radii (Fig. 5). Initially the ratio is close to unity indicating that gas motion in the disc-like object is affected by the angular momentum. This also leads to a deviation from the free-fall accretion rate for the simulation time  $t \in (7-14)$  kyr, which would further increase in case of no angular momentum. After the disc becomes unstable and further protostars form, the angular momentum is transferred efficiently resulting in a decreasing ratio. The low central accretion rates can therefore not be explained by an angular momentum barrier that inhibits the gas flow to smaller radii. A plot of the angular momentum of the gas as a function of enclosed mass for different times is shown in Appendix A (Fig. A1).

In addition we analyse which accretion shielding is dominant in different regions of the cloud. In Fig. 6 we plot the relative velocity of the protostars to the surrounding gas within a radius of  $r_{\text{sur}} = 100 \text{ au} = 2.5 r_{\text{accr}}$  around the protostar. For all times the velocities range from supersonic velocities in the centre of the cloud down to small relative velocities of the order of the speed of sound in the outskirts, indicating that the accretion shielding in the centre follows equation (5), whereas in the outskirts, it is better described by equation (6). As expected, both cases of the accretion shielding effects apply. In the central region, the shielding therefore becomes less efficient with an increasing number of protostars. In contrast, the protostars in the outskirts of the cluster are much more efficient in shielding the accretion flow. In addition to the larger shielded fraction, the shielding at larger distances from the centre becomes even more efficient, because the protostars form along the dense filaments that channel the accretion streams. The area of the strongest accretion flow then coincides with the position of the

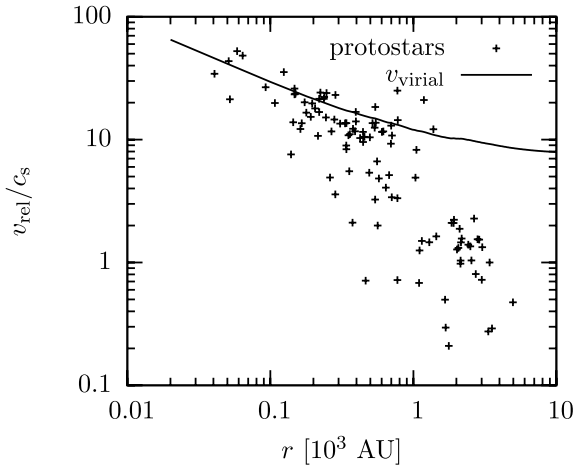


**Figure 6.** Relative velocity between the protostars and the surrounding gas within a radius of  $r_{\text{surr}} = 100$  au around every protostar as a function of distance from the centre of the cluster  $r$  for one snapshot at  $t = 25$  kyr. The plots for different times look very similar. The relative velocity decreases for larger radii ranging from supvirial velocities in the centre down to subvirial velocities of the order of the sound speed at large distances from the centre.

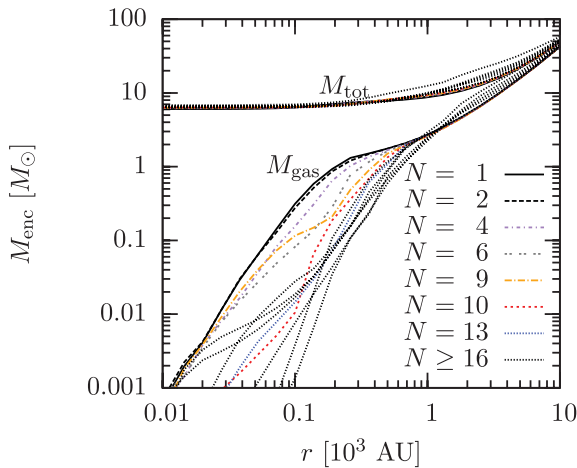


**Figure 7.** Enclosed masses as a function of radius for the total mass (gas and protostars) and the gas mass. The gas is only a small fraction of the total mass in the centre and decreases strongly after the formation of multiple protostars.

protostars that move with the gas flow. As a result, the total gas mass in the centre of the cluster is very small. Fig. 7 shows the total enclosed mass (gas and protostars) as well as the enclosed gas mass as a function of radius. The gas mass is only a small fraction of the total mass and decreases strongly in the centre after the formation of multiple objects. Therefore the central accretion rate is low in spite of a less efficient accretion shielding. The gas is already accreted further out before it reaches the less shielded region.

Depending on the definition of the centre of the cluster (position of the most massive protostar, centre of mass of the protostars, centre of mass including protostars and gas), the most massive protostar is not located exactly at the centre of the cluster. In addition, the interaction with other protostars leads to small displacements during the simulation. Neglecting the fact that only little mass is left in the centre of the cluster, it could be possible that the low accretion rates on to the protostars in the central region arise from these

displacements, if the protostar escapes from a collimated accretion stream. In order to verify that the central stars are really shielded, we need to analyse the motions of the central stars relative to the surrounding gas. We calculate the relative velocity dispersion of the gas with respect to the most massive protostar within a radius of 1000 au around it, covering the vast majority of the entire cluster. We find velocity dispersions ranging from  $\sigma/c_s = 5.4$  to 10.6, resulting in a total time for the gas to reach the central star of 1.7–3.3 kyr after entering the sphere of 1000 au. This time is only 5–10 per cent of the simulated time. Given the low angular momentum in the centre of the cluster (Fig. 5), the available gas has enough time to reach the most massive star regardless of displacements.

### 3.4 Filamentary accretion mode

If the formation of a cluster is not dominated by a disc-like structure but by filaments, the formation scenario of protostars is different (see e.g. Banerjee & Pudritz 2006). The initial density profiles with a flat core need more time to form Jeans-unstable regions. During this time, the turbulence can form filaments in which protostellar condensations form next to each other along the densest part of the filament. The column density plots in Fig. 8 show a time evolution of the filamentary collapse. During their formation, the protostars inherit the motion of the parental filament and move with the gas flow. With increasing proximity to other protostars, their attraction as an  $N$ -body system becomes stronger than the force between protostars and gas. The protostars then dynamically decouple from the filaments and accumulate in the central region in a more spherically symmetric configuration rather than in a flat or string-like structure. The initial filaments get dispersed in the central region, because the  $N$ -body system efficiently stirs the gas. The formation of the first protostars is shown in the column density plots in Fig. 8. The mass accretion in this formation mode is plotted in Fig. 9. Note that Fig. 8 only covers a small time range at the beginning of the cluster formation, whereas Fig. 9 covers the entire simulation time after the formation of sink particles.

During the first  $\sim 6$  kyr after the first protostar has formed, the accretion rate on to the most massive protostar stays roughly constant. About 100 sink particles form along the main filaments within this time. Initially, most protostars can accrete gas from both sides of the filamentary arm, resulting in a high accretion rate. Despite the fact that the total accretion rate increases by a factor of  $\sim 10$ , the average accretion rate gradually drops by about one order of magnitude, because this mass flow is distributed among  $\sim 100$  protostars. This is in contrast to the set-up PL15-m-2, where the global accretion rate suddenly drops. As the set-up is less concentrated, the Keplerian specific angular momentum of the gas with respect to the centre of the nascent cluster is significantly lower than in the PL15-m-2 case. None the less, the ratio  $j_{\text{gas}}/j_{\text{Kepler}}$  (Fig. 5) is even smaller than in the disc-like accretion mode (Fig. 10), indicating that the gas motion is not restricted by the angular momentum barrier. A plot of the angular momentum of the gas as a function of enclosed mass for different times is shown in Appendix A (Fig. A2).

The lower central mass concentration allows for extended filaments and the formation of protostars at larger distances from the centre of the cluster. The relative velocity between the protostars and the surrounding gas (Fig. 11) drops significantly for larger radii, but is closer to the virial velocity for this set-up in comparison to the disc-like structure. The global cluster dynamics should therefore correspond to the shielding relation in equation (5). However, the relative velocities in the outskirts of the cluster are of the order of the speed of sound which marks the transition between the two extreme

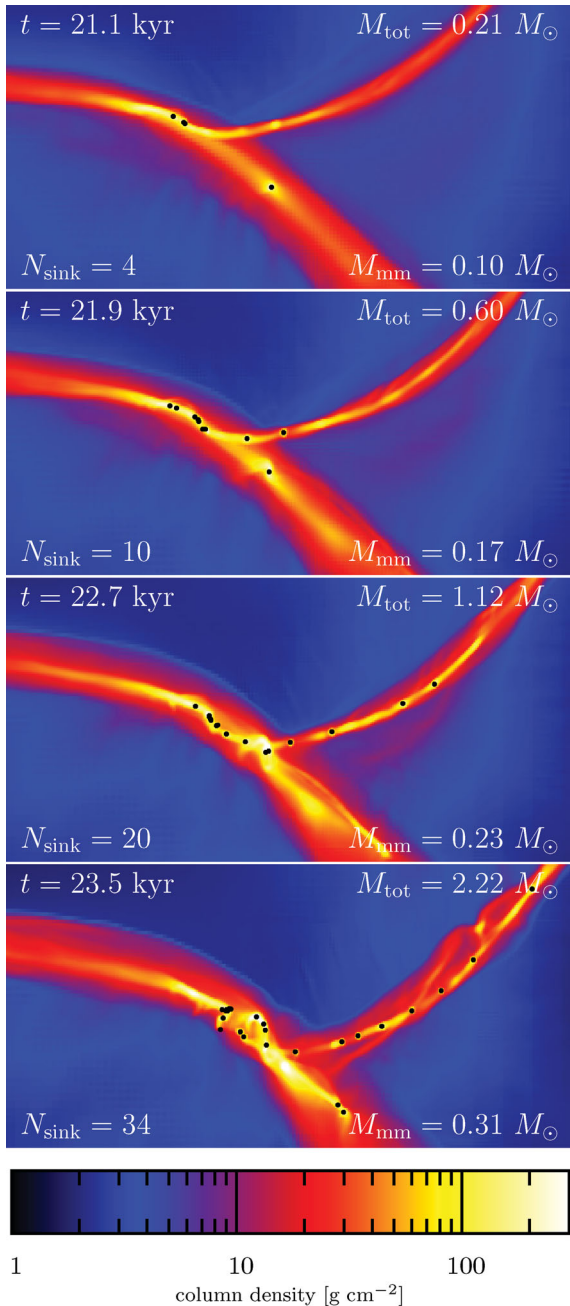


**Figure 8.** Column density plots of the central filament in BE-m-2. The sink particles form in the filament and remain there while converging to the centre of the cluster. The closer the protostars approach each other, the stronger decoupled is their motion from the motion of the filament. The images span roughly  $4000 \times 2000$  au.

shielding cases. In addition, the gas distribution in the filamentary structure strongly deviates from spherical symmetry. The protostars in the outskirts of the nascent cluster move along the densest part of the filament and can therefore efficiently accrete a significant fraction of the filament mass before they dynamically decouple from the filament. As a consequence, the accretion shielding is more efficient, the more protostars form along the filaments. Similar to the disc-like case, the gas content in comparison to the total mass is very low in the central region of the cluster (Fig. 12). Overall, the more protostars accumulate in the central region forming a cluster, the more efficient is the accretion shielding effect. In the case of the

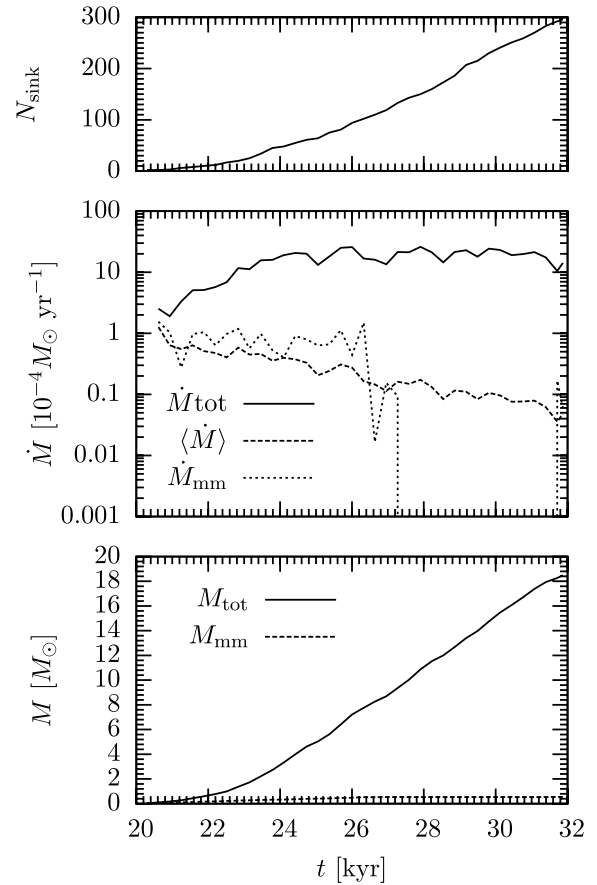


**Figure 9.** Same as Fig. 1 but for the simulation BE-m-2 (filamentary accretion).

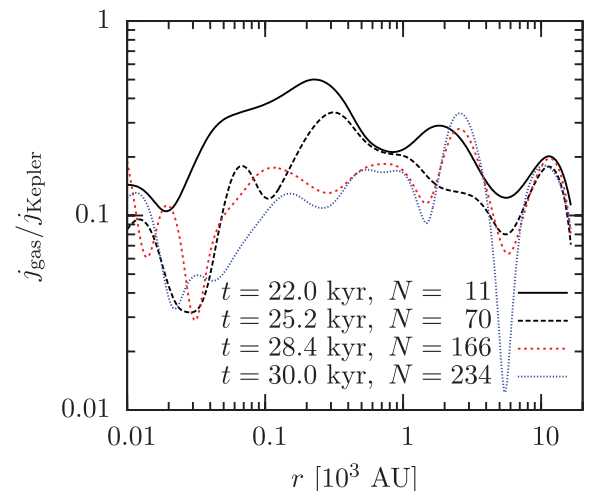


**Figure 10.** Same as Fig. 5 but for set-up BE-m-2 (filamentary accretion).

most massive sink particle in BE-m-2, accretion is entirely shut off for  $t \gtrsim 27$  kyr.

### 3.5 Mass evolution of all runs

In general, the formation scenario of protostars in dense clusters will be a mixture of star formation in a disc and filaments, where the above examples are extremes. However, in all simulated cases, the formation of multiple protostars finally leads to a shielding



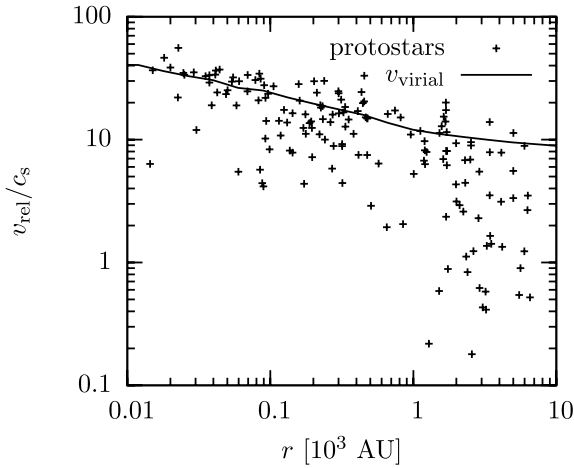


**Figure 11.** Same as Fig. 6 but for set-up BE-m-2 (filamentary accretion) at  $t = 28$  kyr.

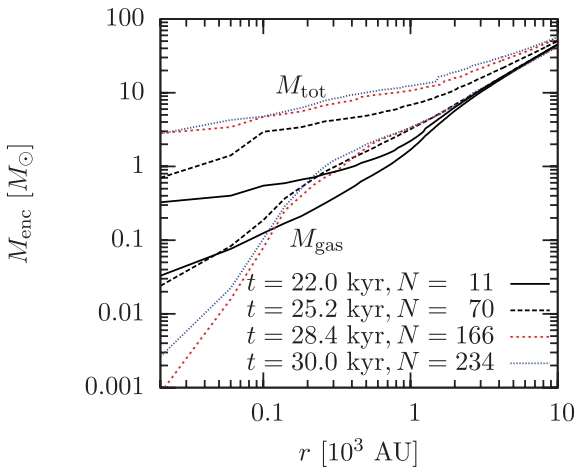


**Figure 12.** Same as Fig. 7 but for BE-m-2 (filamentary accretion).

effect in the formed cluster. Fig. 13 shows the mass evolution of the most massive protostars of all clusters combined, Figs 14–16 show the mass evolution of the 20 most massive sink particles for each simulation. In the case of an initially uniform density (TH, Fig. 14), the two main subclusters for each run (TH-m-1 and TH-m-2) were evaluated separately. The corresponding accretion plots for the most massive sink particle are very similar to the ones shown in Figs 1 and 9. Despite different formation scenarios, all set-ups show very similar structures and emphasize the starvation effect on the most massive protostars, which are located preferentially closer to the centre of the cluster than low-mass companions.

Depending on the formation time, the formation location and the accretion rate over time, the mass of the most massive protostar in relation to the mass of the other objects or the entire ensemble of protostars in the cluster might differ for different set-ups and initial conditions. Fig. 17 shows the mass of the most massive sink particle,  $M_{\text{mm}}$ , in relation to the total mass confined in sink particles,  $M_{\text{tot}}$ . The set-ups with strong initial mass concentrations (PL15) form an early protostar that stays the only sink particle for a significant part of the total simulation. After the formation of subsequent protostars, the mass of the central massive one stays almost constant due to the starvation effect. The mass relations of all PL15 set-ups therefore bend upwards. In the set-ups with initially flat density distribution, the mass of the most massive protostar roughly follows a relation

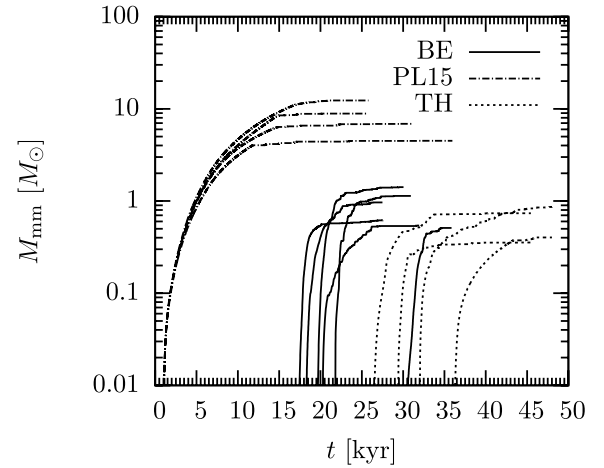


**Figure 13.** Mass evolution of the most massive protostar for all simulated clusters. In all cases the mass curves flatten significantly at the late-time evolution of the simulation. For a detailed mass analysis of each set-up, see Figs 14–16.

$M_{\text{mm}} \propto M_{\text{tot}}^{2/3}$ , but with remarkable scatter. The fact that the difference in mass between the most massive and the other stars is much less, leads to a stronger impact of  $N$ -body interactions on the location of the most massive protostar within the cluster. While the very massive central stars in the PL15 runs remain within the accretion shielded area of the cluster, the most massive stars in the BE runs and in the subclusters of the TH set-ups follow larger orbits where they leave and re-enter the shielded area alternately. Whenever the most massive sink particle gains further mass, either by leaving the accretion shielded area or experiencing episodic accretion, the curve flattens. Entering the accretion shielded volume of the cluster, the most massive object gets starved of material and its accretion stops. As the whole cluster continues to grow, the curves bend up.

#### 4 DISCUSSION

Two accretion models are widely discussed in the literature: (1) the monolithic collapse and (2) competitive accretion and fragmentation-induced starvation, where mutual dynamical interactions of accreting protostars play a key role in shaping the final mass distribution. The monolithic collapse model is based on the apparent similarity of the core mass function (Motte, Andre & Neri 1998; Johnstone et al. 2000; Johnstone, Matthews & Mitchell 2006; Lada et al. 2008) and the stellar IMF (Kroupa 2002; Chabrier 2003). It relies on a direct mapping of cores to stars with a constant efficiency factor for the collapse of a single core into a single stars or at most a binary system. A major caveat in this model is the collapse of very massive cores. The amount of turbulent energy deposited in these cores is likely to cause the core to fragment into many objects. This work and especially Paper I demonstrate that only strongly concentrated density profiles may prevent further fragmentation in an isothermal environment. Radiation feedback tends to reduce the degree of fragmentation, but still cannot prevent the collapsing core from fragmenting into many protostars (Krumholz et al. 2007; Bate 2009; Peters et al. 2010a). Likewise magnetic fields support the agglomeration of larger masses. However, even magnetized cores fragment into smaller objects (Ziegler 2005; Hennebelle & Teyssier 2008; Banerjee et al. 2009; B  rzle et al. 2011; Hennebelle et al. 2011; Peters et al. 2011; Seifried et al. 2011). The degree of fragmentation and the resulting dynamical

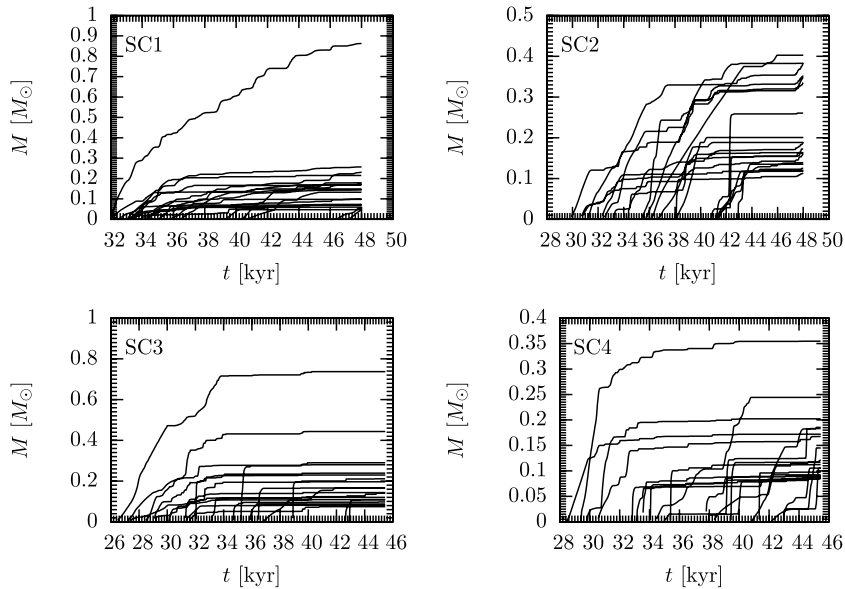


**Figure 14.** Mass evolution of each sink particle for the four main subclusters in the TH set-ups. The upper two plots correspond to the biggest subclusters (SC1, SC2) in run TH-m-1. The lower plots (SC3, SC4) are the main subclusters in TH-m-2, respectively. The most massive particles are located closer to the centre of mass and thus experience an efficient starvation effect, which can be seen in the low increase in mass.

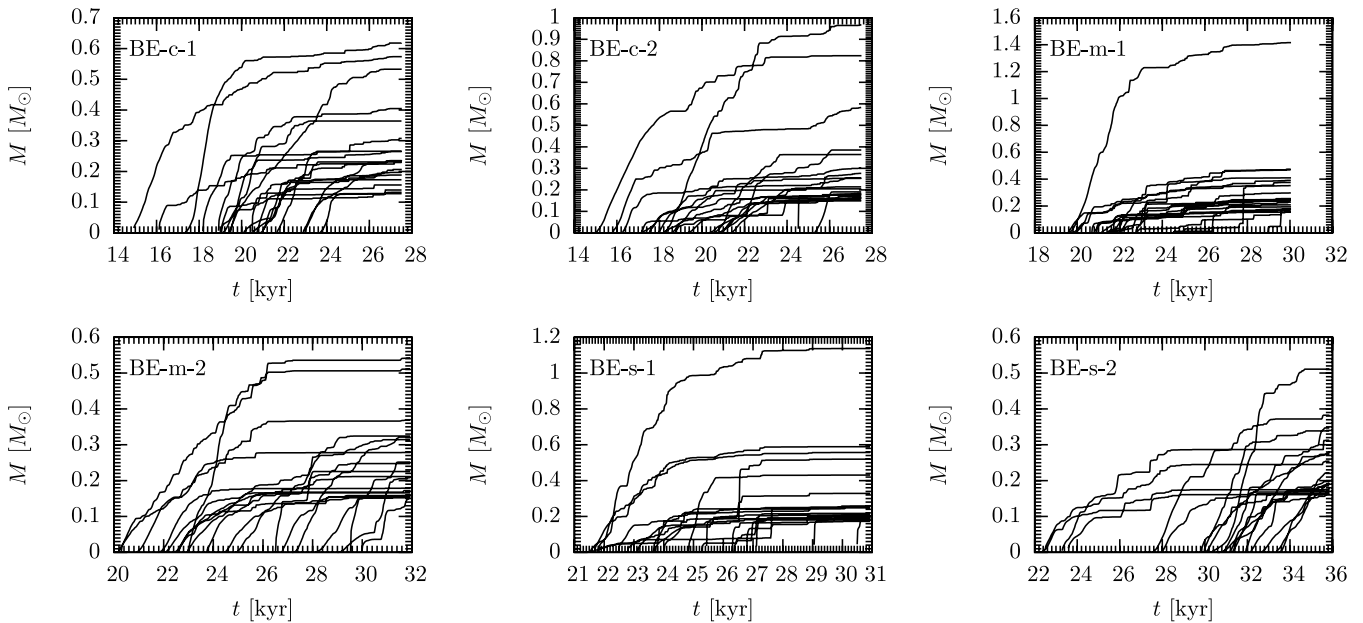


**Figure 15.** Same as Fig. 14 but for the BE set-ups.

accretion in our simulated dense clusters significantly differ from the monolithic collapse model. The fragmentation is suppressed only for highly concentrated density profiles and weak initial turbulent motions (see Paper I). Apart from the fragmentation of the gas, the assumption of a monolithic collapse leads to a time-scale problem that is likely to destroy the apparent similarity of the IMF and the core mass function (Clark, Klessen & Bonnell 2007; Smith, Clark & Bonnell 2008).

In competitive accretion (Bonnell et al. 2001a,b; Bonnell & Bate 2002; Bate & Bonnell 2005), the cloud first fragments down to objects with masses close to the opacity limit, which then start to accrete and build up the initial mass function. The accretion rates are

mainly determined by the position of the protostar in the cluster. The gravitational potential funnels gas to the centre of the cluster, leading to higher accretion rates on to the most central objects, located close to the centre of the potential well. Thus, central protostars can grow to the most massive ones. The more massive a star, the faster it can dynamically migrate to the centre of mass, continuously ensuring a gravitationally privileged position. Assuming a negligible impact of the surrounding protostars on the global mass accretion, the most massive stars continue to accrete at a higher accretion rate. As soon as the impact of further fragmentation influences the global accretion process, the central accretion rates may vary significantly, as it is described in the fragmentation-induced starvation model.

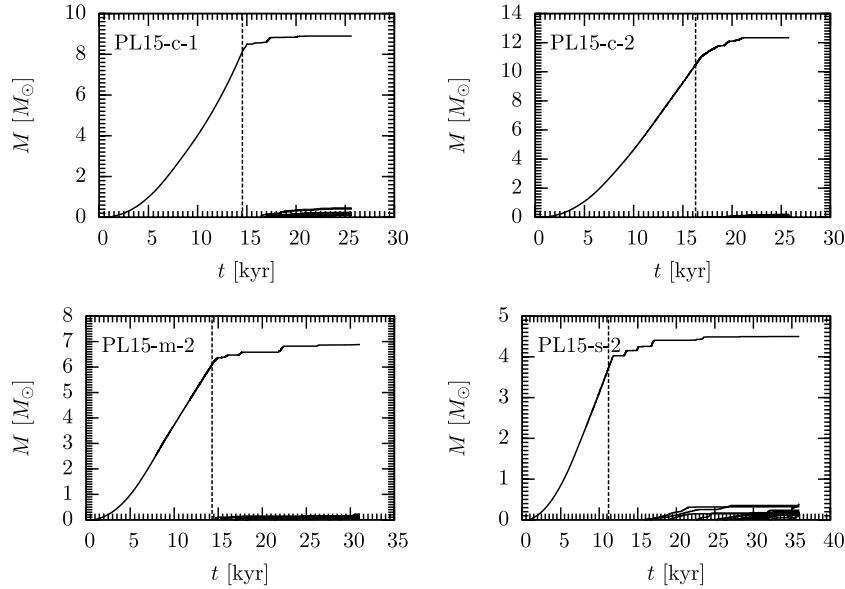


**Figure 16.** Same as Fig. 14 but for the PL15 set-ups. Note that the masses are plotted in linear scale in order to better see the starvation effect, which starts after the formation of the second sink particle (vertical lines).

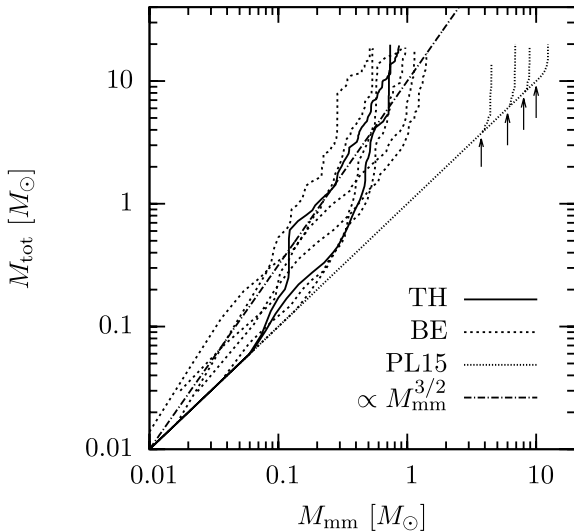


**Figure 17.** Relation of the most massive star in the cluster to the total cluster mass. Note that in the PL15 case, secondary sink particles form very late in the simulation (indicated by the arrows), which explains the large range in mass with a slope of unity.

In competitive accretion, the mass of the most massive star is related to the total stellar mass as  $M_{\text{mm}} \propto M_{\text{tot}}^{2/3}$  (Bonnell, Vine & Bate 2004). This relation was assumed to be an indicator for this accretion model (Krumholz & Bonnell 2009) and is in agreement with observations (Weidner & Kroupa 2006; Weidner, Kroupa & Bonnell 2010). However, as we discuss below, fragmentation-induced starvation can lead to the same behaviour. This relation is therefore not a unique signpost of competitive accretion.

Intermediate scenarios between the two extreme models are also reported (e.g. Peretto, André & Belloche 2006; Wang et al. 2010), in which the formation model depends on the mass of the star. Low-

mass objects form via local collapse, while massive protostars and their dense proximity accumulate gas from the global environment.

Recent numerical models of star cluster formation indicate that the competitive accretion model in its original flavour (Klessen & Burkert 2000, 2001; Bonnell et al. 2001a,b; Bonnell & Bate 2002; Bate & Bonnell 2005) needs re-interpretation. The suggestion of higher central accretion rates due to the gravitationally privileged position changes once the formed fragments around the centre of the collapsing area have a significant impact on the global gas accretion process. The infalling gas may be branched off and either be accreted on to these objects or dynamically redirected before reaching the centre of the cluster. Peters et al. (2010c) found a strong impact of subsequent fragmentation on the accretion flow in a  $1000 M_{\odot}$  rotating core including radiative feedback, but without initial turbulence. The accretion rate on to the central object drops significantly. Instead of growing further, the central protostar is starved of material. Despite this significantly different accretion behaviour, they also found masses in the simulation in good agreement with the relation  $M_{\text{mm}} \propto M_{\text{tot}}^{2/3}$ , ruling out this relation as evidence for competitive accretion. As they do not apply turbulent motions, but only solid body rotation to the initial cloud, they focus on the starvation effect in disc-like conditions rather than in filamentary structures. Because of the missing turbulence, their disc-like structure does not evolve into a volume-filling cluster, but remains a flattened structure. A disc provides a smaller effective area through which gas can flow towards the centre. In a cluster with random protostellar trajectories, the effective accretion area is much larger. Therefore, from simple geometrical arguments, it is much more difficult to shield the central area from accretion flows.

However, we find that protostars in the outer region of the cluster form along the densest part of extended filaments, which allows them to accrete much more mass than in an idealized spherically symmetric set-up. In addition to that, we observe significantly smaller relative velocities between the protostars and the immediate surrounding gas for protostars at larger distances from the centre of the cluster. This increases their geometrical accretion cross-section, expressed by the Bondi–Hoyle accretion radius. Altogether, the

accretion in the central region of the cluster is influenced by efficiently shielding protostars located at the position of the accretion flow. As a result, even a relatively small number of surrounding stars are sufficient to provide an efficient starvation effect in a volume-filling cluster environment.

One caveat of the presented simulations is the missing feedback from the stars that are formed first in the clusters. The gas stays isothermal and therefore tends to fragment much more quickly than with heating of the gas. Including this effect, the number of protostars is expected to be smaller. The starvation effect on the central objects in the protostellar cluster might thus be overestimated, especially in a turbulent volume-filling cluster, where gas can fall into the central region from all directions. However, Peters et al. (2010c) found that the number of protostars in simulations including radiative feedback is roughly half of the number of protostars in an isothermal calculation. As the total number of sink particles in our simulations is much larger than 100, and additionally, the starvation effect can already be seen with a relatively small number of competing protostars, we do not expect the shielding effect to completely vanish in the non-isothermal case. As long as there is some fragmentation, the fragments are likely to shield the central massive star from accretion, irrespective of whether radiation feedback is included or not. Likewise do magnetic fields tend to reduce the degree of fragmentation, but still do not prevent the cloud from fragmenting (Hennebelle et al. 2011; Peters et al. 2011).

Finally, we want to point to recent studies by Kruijssen et al. (2011). They analysed the substructure within clusters as well as the dynamical state of the stellar cluster when gas expulsion becomes important, i.e. at a slightly later stage of the evolution of the cluster. Analysing the simulations of Bonnell, Bate & Vine (2003) and Bonnell, Clark & Bate (2008), they find that the stellar system quickly reaches a globally virialized state if the gas potential is excluded and the stellar system is followed with pure  $N$ -body dynamics. Their results support the evolutionary picture of the formation of protostars that we see in our simulations. New protostars that form at larger radii from the centre of the cluster in gas-dominated regions have subvirial velocities. As soon as they decouple from the gas motion and move to the central gas-poor environment, they quickly virialize.

## 5 SUMMARY AND CONCLUSION

We performed simulations of collapsing molecular gas clouds with a total mass of  $100 M_{\odot}$  and a diameter of 0.2 pc. We varied the initial density profile as well as the turbulent supersonic velocity field and analysed the fragmentation process and the accretion on to nascent protostars. Most clouds, especially the ones with initially less centrally concentrated density profiles undergo fragmentation and form compact stellar clusters. We studied the accretion process in these clusters with the following conclusions.

- (i) All clusters show strong and fast dynamical interactions between the protostars. During the formation time of the cluster, the protostars complete several orbits in the parental cluster. The mass accretion process can thus not be described by a monolithic collapse model.
- (ii) Fragmentation and formation of multiple protostars strongly influence the subsequent accretion flow in the entire cluster. Gas that falls towards the centre of the cluster is efficiently accreted on to protostars that are located at larger radii from the cluster centre. As a consequence, the central region is effectively shielded

from further accretion and none of the central objects can sustain its initially high accretion rate. In all cases the observed decrease of the central accretion rate is due to the efficient shielding by secondary protostars. A significant starvation effect due to angular momentum and a resulting radial barrier can be excluded.

(iii) In set-ups with initial flat density distributions, the mass of the most massive protostar,  $M_{\text{mm}}$ , scales with the total cluster mass,  $M_{\text{tot}}$ , like  $M_{\text{mm}} \propto M_{\text{tot}}^{2/3}$ , as originally proposed as a probe for competitive accretion. This relation is a common feature to both dynamical accretion models and cannot be used to distinguish between competitive accretion and fragmentation-induced starvation, a conclusion that was already reached by Peters et al. (2010b).

(iv) The accretion process does not differ between density profiles that form only one main cluster (power-law profiles, Bonnor–Ebert density distribution) and set-ups that form multiple subclusters (uniform density profile). In both, the central clusters as well as the disconnected subclusters, we find fragmentation-induced starvation to work in the central region of the cluster.

## ACKNOWLEDGMENTS

We thank Thomas Peters for many interesting discussions and comments as well as the referee, Ian Bonnell, for very useful comments and suggestions to improve the depiction of the relevant physics. PG acknowledges supercomputer grants at the Jülich Supercomputing Centre (NIC 3433) and at the CASPUR Centre (cmp09-849). PG and CF are grateful for financial support from the International Max Planck Research School for Astronomy and Cosmic Physics (IMPRS-A) and the Heidelberg Graduate School of Fundamental Physics (HGSFP), funded by the Excellence Initiative of the Deutsche Forschungsgemeinschaft (DFG) under grant GSC 129/1. CF, RB and RSK acknowledge financial support from the Landesstiftung Baden-Württemberg via their programme *Internationale Spitzenforschung II* (grant P-LS-SPII/18) and from the German Bundesministerium für Bildung und Forschung via the ASTRONET project STAR FORMAT (grant 05A09VHA). CF also acknowledges funding from the European Research Council under the European Community(tm)s Seventh Framework Programme (FP7/2007-2013 grant agreement no. 247060) and from the Australian Research Council for a Discovery Projects Fellowship (grant no. DP110102191). PG and RB acknowledge funding of Emmy Noether grant BA 3706/1-1 by the DFG. RB is thankful for subsidies from the FRONTIER initiative of the University of Heidelberg. RSK acknowledges subsidies from the DFG under grants no. KL1358/10 and KL1358/11, the Sonderforschungsbereich SFB 881 *The Milky Way System* as well as from a Frontier grant of Heidelberg University sponsored by the German Excellence Initiative. This work was supported in part by the US Department of Energy contract no. DEAC-02-76SF00515. The FLASH code was developed in part by the DOE-supported Alliances Center for Astrophysical Thermonuclear Flashes (ASC) at the University of Chicago.

## REFERENCES

- Banerjee R., Pudritz R. E., 2006, *ApJ*, 641, 949
- Banerjee R., Vázquez-Semadeni E., Hennebelle P., Klessen R. S., 2009, *MNRAS*, 398, 1082
- Bastian N., Covey K. R., Meyer M. R., 2010, *ARA&A*, 48, 339
- Bate M. R., 2009, *MNRAS*, 392, 590
- Bate M. R., Bonnell I. A., 2005, *MNRAS*, 356, 1201
- Baumgardt H., Klessen R. S., 2011, *MNRAS*, 413, 1810
- Bertoldi F., 1989, *ApJ*, 346, 735



Bertoldi F., McKee C. F., 1990, *ApJ*, 354, 529  
 Bondi H., 1952, *MNRAS*, 112, 195  
 Bondi H., Hoyle F., 1944, *MNRAS*, 104, 273  
 Bonnell I. A., Bate M. R., 2002, *MNRAS*, 336, 659  
 Bonnell I. A., Bate M. R., Clarke C. J., Pringle J. E., 2001a, *MNRAS*, 323, 785  
 Bonnell I. A., Clarke C. J., Bate M. R., Pringle J. E., 2001b, *MNRAS*, 324, 573  
 Bonnell I. A., Bate M. R., Vine S. G., 2003, *MNRAS*, 343, 413  
 Bonnell I. A., Vine S. G., Bate M. R., 2004, *MNRAS*, 349, 735  
 Bonnell I. A., Clark P., Bate M. R., 2008, *MNRAS*, 389, 1556  
 Bressert E. et al., 2010, *MNRAS*, 409, L54  
 B r  le F., Clark P. C., Stasyszyn F., Greif T., Dolag K., Klessen R. S., Nielaba P., 2011, *MNRAS*, 412, 171  
 Chabrier G., 2003, *PASP*, 115, 763  
 Clark P. C., Klessen R. S., Bonnell I. A., 2007, *MNRAS*, 379, 57  
 Colella P., Woodward P. R., 1984, *J. Comput. Phys.*, 54, 174  
 Commer on B., Hennebelle P., Audit E., Chabrier G., Teyssier R., 2010, *A&A*, 510, L3  
 Elmegreen B. G., Lada C. J., 1977, *ApJ*, 214, 725  
 Federrath C., Klessen R. S., Schmidt W., 2008, *ApJ*, 688, L79  
 Federrath C., Banerjee R., Clark P. C., Klessen R. S., 2010a, *ApJ*, 713, 269  
 Federrath C., Roman-Duval J., Klessen R. S., Schmidt W., Mac Low M., 2010b, *A&A*, 512, A81  
 Fryxell B. et al., 2000, *ApJS*, 131, 273  
 Girichidis P., Federrath C., Banerjee R., Klessen R. S., 2011, *MNRAS*, 413, 2741 (Paper I)  
 Hennebelle P., Ciardi A., 2009, *A&A*, 506, L29  
 Hennebelle P., Fromang S., 2008, *A&A*, 477, 9  
 Hennebelle P., Teyssier R., 2008, *A&A*, 477, 25  
 Hennebelle P., Commer on B., Joos M., Klessen R. S., Krumholz M., Tan J. C., Teyssier R., 2011, *A&A*, 528, A72  
 Heyer M. H., Brunt C. M., 2004, *ApJ*, 615, L45  
 Johnstone D., Wilson C. D., Moriarty-Schieven G., Joncas G., Smith G., Gregersen E., Fich M., 2000, *ApJ*, 545, 327  
 Johnstone D., Matthews H., Mitchell G. F., 2006, *ApJ*, 639, 259  
 Klessen R. S., 2001, *ApJ*, 556, 837  
 Klessen R. S., Burkert A., 2000, *ApJS*, 128, 287  
 Klessen R. S., Burkert A., 2001, *ApJ*, 549, 386  
 Klessen R. S., Heitsch F., Mac Low M.-M., 2000, *ApJ*, 535, 887  
 Kroupa P., 2001, *MNRAS*, 322, 231  
 Kroupa P., 2002, *Sci*, 295, 82  
 Kruijssen J. M. D., Maschberger T., Moeckel N., Clarke C. J., Bastian N., Bonnell I. A., 2011, *MNRAS*, doi:10.1111/j.1365-2966.2011.20037.x (arXiv:1109.0986)  
 Krumholz M. R., Bonnell I. A., 2009, in Chabrier G., ed., *Models for the Formation of Massive Stars*. Cambridge Univ. Press, Cambridge, p. 288  
 Krumholz M. R., Klein R. I., McKee C. F., 2007, *ApJ*, 656, 959  
 Lada C. J., Bergin E. A., Alves J. F., Huard T. L., 2003, *ApJ*, 586, 286  
 Lada C. J., Muench A. A., Rathborne J., Alves J. F., Lombardi M., 2008, *ApJ*, 672, 410  
 Larson R. B., 1981, *MNRAS*, 194, 809  
 McKee C. F., Ostriker E. C., 2007, *ARA&A*, 45, 565  
 McKee C. F., Tan J. C., 2002, *Nat*, 416, 59  
 McKee C. F., Tan J. C., 2003, *ApJ*, 585, 850  
 Mac Low M.-M., Klessen R. S., 2004, *Rev. Modern Phys.*, 76, 125  
 Motte F., Andre P., Neri R., 1998, *A&A*, 336, 150  
 Olson K. M., MacNeice P., Fryxell B., Ricker P., Timmes F. X., Zingale M., 1999, *BAAS*, 31, 1430  
 Peretto N., Andr   P., Belloche A., 2006, *A&A*, 445, 979  
 Peters T., Banerjee R., Klessen R. S., Mac Low M., Galv  n-Madrid R., Keto E. R., 2010a, *ApJ*, 711, 1017  
 Peters T., Mac Low M., Banerjee R., Klessen R. S., Dullemond C. P., 2010b, *ApJ*, 719, 831  
 Peters T., Klessen R. S., Mac Low M., Banerjee R., 2010c, *ApJ*, 725, 134  
 Peters T., Banerjee R., Klessen R. S., Mac Low M., 2011, *ApJ*, 729, 72  
 Price D. J., Bate M. R., 2007, *Ap&SS*, 311, 75  
 Scalo J. M., 1986, *Fundamentals Cosmic Phys.*, 11, 1

Scalo J., 1998, in Gilmore G., Howell D., eds, *ASP Conf. Ser. Vol. 142, The Stellar Initial Mass Function (38th Herstmonceux Conference)*. Astron. Soc. Pac., San Francisco, p. 201  
 Schmeja S., Klessen R. S., 2004, *A&A*, 419, 405  
 Seifried D., Banerjee R., Klessen R. S., Duffin D., Pudritz R. E., 2011, *MNRAS*, 417, 1054  
 Smith R. J., Clark P. C., Bonnell I. A., 2008, *MNRAS*, 391, 1091  
 Smith R. J., Longmore S., Bonnell I., 2009, *MNRAS*, 400, 1775  
 Testi L., Sargent A. I., 1998, *ApJ*, 508, L91  
 Truelove J. K., Klein R. I., McKee C. F., Holliman J. H., Howell L. H., Greenough J. A., 1997, *ApJ*, 489, L179  
 Wang P., Li Z., Abel T., Nakamura F., 2010, *ApJ*, 709, 27  
 Weidner C., Kroupa P., 2006, *MNRAS*, 365, 1333  
 Weidner C., Kroupa P., Bonnell I. A. D., 2010, *MNRAS*, 401, 275  
 Whitworth A. P., Bhattal A. S., Chapman S. J., Disney M. J., Turner J. A., 1994, *MNRAS*, 268, 291  
 Ziegler U., 2005, *A&A*, 435, 385  
 Zinnecker H., Yorke H. W., 2007, *ARA&A*, 45, 481

## APPENDIX A: ANGULAR MOMENTUM

In order to see the time evolution of the angular momentum, we show the specific angular momentum as a function of enclosed mass for

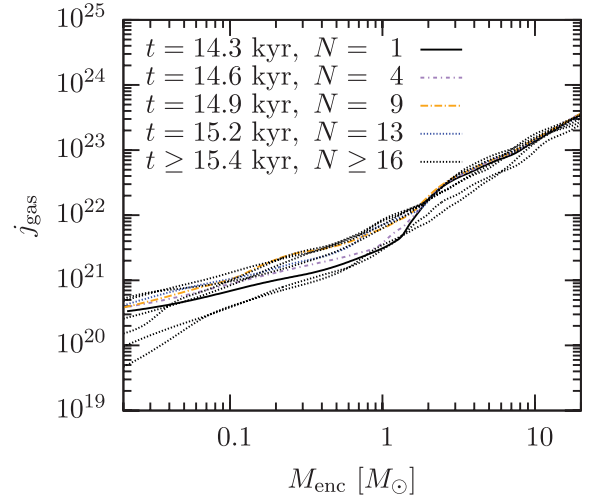


**Figure A1.** Specific angular momentum of the gas as a function of enclosed mass for PL15-m-2. The plot shows temporal changes of the angular momentum of the gas during the formation of the cluster.

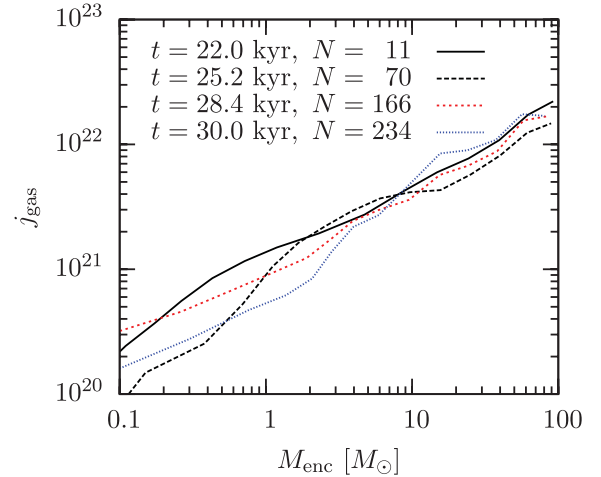


**Figure A2.** Same as Fig. A1 but for set-up BE-m-2.

the set-ups PL15-m-2 and BE-m-2 (Figs A1 and A2). In both cases the angular momentum distribution is exposed to variations of the order of a few up to almost an order of magnitude due to the turbulent interactions and the gas accretion on to protostars. Because of the unstructured motions of the protostars and the random character of the turbulence, the variations do not show systematic changes over

time, i.e. the gas in the cluster can quickly gain angular momentum due to accretion streams or lose it via shocks and dissipation.

This paper has been typeset from a  $\text{\TeX/L\AA\TeX}$  file prepared by the author.